

Development of open-source software mVMC and its applications

Takahiro Misawa, Yuichi Motoyama, and Kota Ido
Institute for Solid State Physics, University of Tokyo
Kashiwa-no-ha, Kashiwa, Chiba 277-8581

Abstract

In this activity report, we overview open-source software mVMC (many-variable variational Monte Carlo), which can perform the variational Monte Carlo calculations with many variational parameters for a wide range of the quantum many-body systems. We also show its recent applications to the high- T_c superconductivity and the quantum spin liquid. In the first part of the report, we explain the basic properties of mVMC including the Monte Carlo sampling method, implemented wavefunctions, optimization methods (the steepest descend method and the stochastic reconfiguration method), and the recent extension to simulations in the grand canonical ensemble. As applications of mVMC, we first show the analysis of the interfaces of the cuprates. A recent experiment shows that the superconducting temperature is pinned at optimal value in the bulk compound at the interfaces of the cuprates ($\text{La}_2\text{CuO}_4/\text{La}_{2-x}\text{Sr}_x\text{CuO}_4$) irrespective of the hole doping ratio. By using mVMC, we solve an effective model for the interfaces and reproduce the anomalous pinning at the interfaces. We also clarify the origin of the pinning is the inter-layer phase separation, which dissolves inner-layer phase separation through the reconstruction of the hole densities around the interfaces. Then, we show the application of mVMC to the quantum spin liquid in the Kitaev model (Kitaev spin liquid). By using the grand canonical ensemble, we show that mVMC can reproduce the Kitaev spin liquid.

1 Introduction

Correlation effects among electrons in solids induce many intriguing phenomena such as the high- T_c superconductivity [1, 2, 3] and the exotic elementary excitations in the quantum spin liquids [4]. To reveal how and why the correlation effects induce such exotic phenomena, it is necessary to develop numerical methods that can accurately treat the correlation effects.

The variational Monte Carlo (VMC) method (for reviews see Refs. [5, 6]) is one of the promising methods for performing accurate analysis of correlated electrons. The VMC method was first used for analyzing the properties of the quantum liquids of He^4 [7] and He^3 [8]. As the optimization of many variational parameters is a difficult problem, the number of variational parameter was limited up to around ten or one hundred (10^2) for a long time. After the proposal of the stochastic optimization (SR) method [9, 10] proposed by Sorella, we can optimize more than one thousand (10^3) variational parameters. By using powerful supercomputers and the improved SR method [11], it is now possible to optimize more than several hundred thousand (10^5) variational parameters.

In the 2016 fiscal year, we have developed open-source software mVMC [12, 13, 14], which can perform the many-variable variational Monte Carlo method for a wide range of Hamiltonians of correlated fermion systems. The development of mVMC has

been supported by “Project for advancement of software usability in materials science (PASMS)” [15], which is managed by the center of the supercomputer at Institute for Solid State Physics. We note that the code of mVMC [16, 17] was originally written by Daisuke Tahara, who was a graduate student in Imada group in the University of Tokyo. Based on his code, several people including authors have improved and added new functions in mVMC.

In the past decade, mVMC has been applied to a wide range of quantum many-body systems such as the frustrated Heisenberg models [18, 19], the Hubbard models at half filling [16, 17], the doped Hubbard models [16, 20, 21, 22], and the Kondo-lattice models [23, 24]. mVMC has also been applied to more realistic Hamiltonians such as ab initio low-energy Hamiltonians for the iron-based superconductors [25, 26, 27, 28], the organic conductor [29], and the cuprates [30, 31]. As we show later, mVMC has been applied to the interfaces of cuprates (multi-layer Hubbard model) [32]. It is also possible to apply mVMC to the spin-orbit coupled systems including the Kitaev spin liquid [33, 34, 35, 36] and the systems with electron-phonon couplings [37, 38]. Furthermore, recent studies reveal that mVMC can be used for the non-equilibrium calculations [39, 40] and the finite-temperature calculations [41].

In this activity report, we briefly explain the basic properties of mVMC and its recent applications to strongly correlated electron systems. This report is organized as follows: In Sec. 2, we detail the models that can be treated by mVMC, Monte Carlo sampling method, wavefunctions implemented in mVMC, and optimization methods. We also describe the recent implementation of the grand canonical ensemble in mVMC in Sec. 2.5. In Sec. 3, we show applications of mVMC to the interfaces of the cuprates [32], and the Kitaev model [36]. Section 4 is devoted for summary and discussions.

2 Basic of mVMC

In this section, we describe the models that can be treated by mVMC, Monte Carlo sampling in the VMC method, and the wavefunctions implemented in mVMC. We detail the stochastic reconfiguration method, which enables us to optimize many variational parameters. We also explain how to perform VMC simulations in the grand canonical ensemble, which has been recently implemented in mVMC. We note that VMC simulations in the grand canonical ensemble cannot be performed in the released version, which will be available in near future.

2.1 Model

By using mVMC, users can treat the general Hamiltonians defined as

$$\mathcal{H} = \mathcal{H}_T + \mathcal{H}_I, \quad (1)$$

$$\mathcal{H}_T = - \sum_{I,J} t_{IJ} c_I^\dagger c_J, \quad (2)$$

$$\mathcal{H}_I = \sum_{I,J,K,L} \mathcal{I}_{IJKL} c_I^\dagger c_J c_K^\dagger c_L, \quad (3)$$

where capital characters I, J, K, L denote the site indices including the spin degrees of freedom ($\sigma = \uparrow$ or \downarrow), i.e., $I = (i, \sigma)$, where i represents the i th site. Here, c_I^\dagger (c_I) is the creation (annihilation) operator of an electron on site I . This Hamiltonian includes the arbitrary one-body transfers and two-body interactions in the particle-conserved systems. General one-body potential t_{IJ} represents the hopping between site I and site J . General two-body interaction \mathcal{I}_{IJKL} represents the interaction which annihilates a particle at site J and a particle at site L , and creates a particle at site I and a particle at site K .

As a special case of the general Hamiltonian defined in Eq. (3), we can treat the localized spin Hamiltonian such as the Heisenberg model by prohibiting the doubly occupied sites and the vacancy sites in the Monte Carlo samplings. It is also possible to treat the Kondo-lattice model, where the localized

spins and itinerant electrons coexist. We note the spinless-fermion models can be treated by restricting Monte Carlo samplings in the fully polarized states (e.g., samplings only in $\sigma = \uparrow$ states).

Users of mVMC can perform VMC calculations by preparing one input file whose length is typically less 10 lines for the standard models such as the Hubbard model and the Heisenberg model. Details of user interfaces are shown in Ref. [14]. Tutorials for mVMC and some script files for the standard models can be found in the GitHub repository (mVMC-tutorial) [42].

2.2 Monte Carlo sampling

Here, we explain how the Markov-chain Monte Carlo sampling is used in the VMC method. In the VMC method, the expectation value of the physical quantities A is expressed by

$$\begin{aligned} \langle A \rangle &= \frac{\langle \psi | A | \psi \rangle}{\langle \psi | \psi \rangle} = \sum_x \frac{\langle \psi | A | x \rangle \langle x | \psi \rangle}{\langle \psi | \psi \rangle} \\ &= \sum_x \rho(x) \frac{\langle \psi | A | x \rangle}{\langle \psi | x \rangle}, \end{aligned} \quad (4)$$

$$\rho(x) = \frac{|\langle x | \psi \rangle|^2}{\langle \psi | \psi \rangle}, \quad (5)$$

where $|\psi\rangle$ is a many-body wavefunction and $|x\rangle$ denotes a complete basis such as the real-space configuration.

From Eq. (4), by performing the Markov-chain Monte Carlo sampling with respect to the weight $\rho(x)$, i.e., by generating the real-space configurations according to the weight $\rho(x)$ iteratively, we can evaluate $\langle A \rangle$ as

$$\langle A \rangle \sim \frac{1}{N_{\text{MC}}} \sum_x \frac{\langle \psi | A | x \rangle}{\langle \psi | x \rangle}, \quad (6)$$

where N_{MC} is the number of Monte Carlo samplings. It should be noted that the $\rho(x)$ is obviously positive definitive and the infamous sign problem never appears in the VMC method. In mVMC, we use the Mersenne twister [43] for generating pseudo random numbers.

2.3 Wavefunction

Wavefunctions implemented in mVMC are given as

$$|\psi\rangle = \mathcal{P}\mathcal{L}|\phi_{\text{Pf}}\rangle, \quad (7)$$

where $|\phi_{\text{Pf}}\rangle$ denotes the pair-product wavefunctions, \mathcal{L} denotes the quantum-number projectors such as the total-spin and the momentum projections, and \mathcal{P} denotes the correlation factors such as the Gutzwiller and the Jastrow factors.

Because the details of the quantum-number projectors and the correlation factors are shown in Ref. [14], in this report, we only explain the several variations of the pair-product wavefunction $|\phi_{\text{Pf}}\rangle$. The general form of the pair-product wavefunction is given as

$$|\phi_{\text{Pf}}\rangle = |\phi_{\text{GC}}\rangle = \exp \left[\sum_{I,J} F_{IJ} c_I^\dagger c_J^\dagger \right] |0\rangle, \quad (8)$$

where F_{IJ} is treated as the variational parameters. This is nothing but the generalized Bardeen-Cooper-Schrieffer (BCS) wavefunctions, which include both singlet and triplet pairings. The inner product between $|\phi_{\text{GC}}\rangle$ and $|x\rangle$ is represented as the Pfaffian of a skew-symmetric matrix constructed from the pairing F_{IJ} , which is detailed in Sec. 2.5. Although it is possible to directly treat the general form of the pair-product wavefunction, there is no necessary to use $|\phi_{\text{GC}}\rangle$ for particle-number conserved systems. In other words, we need to employ $|\phi_{\text{GC}}\rangle$ only when the particle-number conservation is explicitly broken in target Hamiltonians.

To treat particle-number conserved systems efficiently, we often use the particle-number fixed wavefunctions defined as

$$|\phi_{\text{Pf}}\rangle = |\phi_{\text{SGC}}\rangle = \left[\sum_{I,J} F_{IJ} c_I^\dagger c_J^\dagger \right]^{N_e/2} |0\rangle, \quad (9)$$

where N_e is the particle number. Furthermore, for systems where the total value of S^z is fixed

to 0, we can use the anti-parallel Pfaffian wavefunction defined as

$$|\phi_{\text{Pf}}\rangle = |\phi_{\text{AP-Pf}}\rangle = \left[\sum_{i,j} f_{ij} c_{i\uparrow}^\dagger c_{j\downarrow}^\dagger \right]^{N_e/2} |0\rangle. \quad (10)$$

Clearly, by employing the restriction on the total value of S^z , the number of variational parameters can be reduced. Thus, to reduce the numerical cost, it is better to impose the restrictions on the pair-product wavefunctions if it is possible.

2.4 Optimization method

The key procedure in the VMC method is how to optimize the variational parameters α to lower the energy E according to the variational principle. As an optimization method, the general gradient method is often used, which is given as

$$\Delta\alpha = \alpha_{\text{new}} - \alpha_{\text{old}} = -\eta X^{-1} \mathbf{g}, \quad (11)$$

$$g_k = \frac{\partial E}{\partial \alpha_k}, \quad (12)$$

where η is a small constant and X is matrix whose dimension is the number of variational parameters. If we choose the identity matrix as X , the optimization method is called the steepest decent (SD) method. As we show later, the SD method do not efficiently work for optimizing many variational parameters.

In the stochastic reconfiguration (SR) method [9, 10], we take X as the overlap matrix S , which is defined as

$$S_{\alpha\beta} = \langle \bar{\psi}_\alpha | \bar{\psi}_\beta \rangle, \quad (13)$$

$$|\bar{\psi}_\alpha\rangle = \frac{\partial |\bar{\psi}\rangle}{\partial \alpha}, \quad (14)$$

$$|\bar{\psi}\rangle = \frac{|\psi\rangle}{\sqrt{\langle \psi | \psi \rangle}}. \quad (15)$$

As it is mentioned in the literature [14, 39, 41, 14, 44], the SR method is nothing but the imaginary-time evolution based on the time-dependent variational principle. As we show

later, the SR method works well for optimization of many-variational parameters. We note the natural gradient method [45] used in the field of the neural network is the same as the SR method (the overlap matrix is called natural gradient in the field of the neural network).

In Fig. 1, we show the optimization processes by the SD method and the SR method by taking 4×4 Hubbard model as an example. For both the random initial state and the initial state made from the unrestricted Hartree-Fock (UHF) solutions, the SR results can reach the ground state faster than the SD results. In our experience, for many variational parameters, the speed of the convergence by the SD method is always slower than the SR method.

2.5 Grand canonical ensemble

The present mVMC package can be applied to a wide range of quantum lattice models. However, only systems where the total number of the particles is fixed are applicable. Due to this restriction, we cannot treat Hamiltonians which does not conserve the number of the particles such as the BCS Hamiltonian.

Recently, we have implemented the new functionality to perform VMC simulations in the grand canonical ensemble (GCE). The employed mean-field part in the trial wavefunction [Eq. (7)] is the generalized BCS wavefunction *without* the particle-number projection, namely

$$|\phi\rangle = \exp \left[\sum_{I,J} f_{IJ} c_I^\dagger c_J^\dagger \right] |0\rangle. \quad (16)$$

Here $I = (i, \sigma)$ and the pairing f_{IJ} is treated as the variational parameters.

We generate Monte Carlo samples in the GCE by using Metropolis-Hastings algorithm. The acceptance probability $p(x \rightarrow y)$ is defined

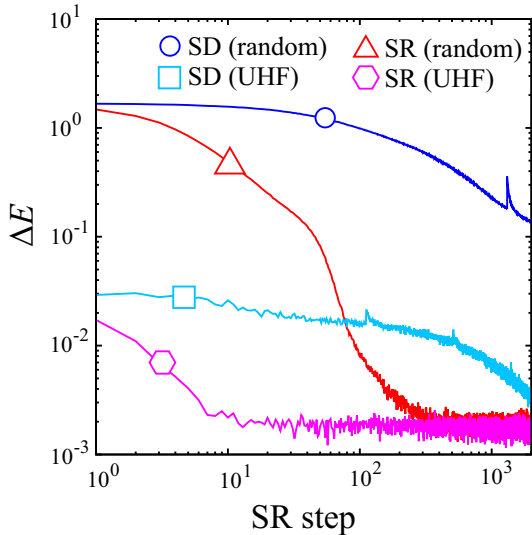


Figure 1: Optimization processes for 4×4 Hubbard model for $U = 4$ and $t = 1$ at half filling with periodic boundary conditions. The relative energy is defined as $\Delta E = (E_{\text{mVMC}} - E_{\text{exact}})/N_s$, where E_{mVMC} (E_{exact}) represents the energy obtained by mVMC (exact diagonalization). N_s denotes the number of sites. We do not impose the sublattice structure in the variational parameters and the number of variational parameters are 266. Random (UHF) means that the initial state of the wavefunctions is prepared by random variational numbers (the UHF solution).

as

$$p(x \rightarrow y) = \min \left(1, \left| \frac{P(y) \langle \phi | y \rangle}{P(x) \langle \phi | x \rangle} \right|^2 \frac{g(x|y)}{g(y|x)} \right), \quad (17)$$

where $g(y|x)$ is the proposal distribution for proposing a new configuration y from a given one x with the total number of the particles $N_e = 2N$. Although $g(y|x)/g(x|y) = 1$ for systems with the fixed particle number, we should be careful to consider the ratio of the proposal distributions $g(y|x)/g(x|y)$ when two particles is added or removed from the old configuration x . This is because the dimension of systems for $2N \pm 2$ is different from that for $2N$. For example, the ratio when a new configuration is

generated by adding two particles is

$$\frac{g(y|x)}{g(x|y)} = \frac{(2N_s - 2N)(2N_s - (2N + 1))}{(2N + 2)(2N + 1)}. \quad (18)$$

The inner product between the BCS wavefunction $|\phi\rangle$ and the real space configuration $|x\rangle$ for $N_e = 2N$ is given as

$$\langle x | \phi \rangle = \text{Pf}[X], \quad (19)$$

$$X_{IJ} = f_{R_I R_J} - f_{R_J R_I}, \quad (20)$$

$$|x\rangle = c_{R_1}^\dagger \cdots c_{R_{2N}}^\dagger |0\rangle. \quad (21)$$

Here, X is a skew symmetric matrix whose dimension is $2N$. It is worth noting that even in the GCE, the fast update techniques for calculations of Pfaffian and inverse matrices can be used when a real-space configuration is updated by adding or removing two particles. In this report, we introduce the fast update scheme when the electron configuration $|x\rangle$ is updated as $|x'\rangle = c_{R_{2N+1}}^\dagger c_{R_{2N+2}}^\dagger |x\rangle$. The skew symmetric matrix X' with the $2N + 2$ dimension is described as

$$X' = \begin{pmatrix} X & B \\ -B^T & C^{-1} \end{pmatrix}, \quad (22)$$

$$B^T = - \begin{pmatrix} f_{R_1 R_{2N+1}} & \cdots & f_{R_{2N} R_{2N+1}} \\ f_{R_1 R_{2N+2}} & \cdots & f_{R_{2N} R_{2N+2}} \end{pmatrix}, \quad (23)$$

$$C^{-1} = \begin{pmatrix} 0 & f_{R_{2N+1} R_{2N+2}} \\ f_{R_{2N+2} R_{2N+1}} & 0 \end{pmatrix}. \quad (24)$$

By using the following lemma

$$\begin{aligned} & \text{Pf} \begin{pmatrix} A & B \\ -B^T & C^{-1} \end{pmatrix} \\ &= \text{Pf} A \times \text{Pf} (C^{-1} + B^T A^{-1} B), \end{aligned} \quad (25)$$

the new Pfaffian $\text{Pf} X'$ can be described as

$$\text{Pf} X' = \text{Pf} X \times \text{Pf} D, \quad (26)$$

$$D = C^{-1} + B^T A^{-1} B. \quad (27)$$

Since $\text{Pf} X$ and X^{-1} have been already known, 2×2 skew symmetric matrix D can be easily

computed and its numerical cost $\mathcal{O}(N^2)$. The inverse matrix X'^{-1} is computed as

$$X'^{-1} = \begin{pmatrix} X'_{11}{}^{-1} & X'_{12}{}^{-1} \\ X'_{21}{}^{-1} & X'_{22}{}^{-1} \end{pmatrix}, \quad (28)$$

$$X'_{11}{}^{-1} = X^{-1} - X^{-1}BDB^T X^{-1}, \quad (29)$$

$$X'_{12}{}^{-1} = -X^{-1}BD^{-1}, \quad (30)$$

$$X'_{21}{}^{-1} = D^{-1}B^T X^{-1}, \quad (31)$$

$$X'_{22}{}^{-1} = D^{-1}, \quad (32)$$

from the LDU decomposition of X' defined in Eq. (22). The numerical cost for evaluation of X'^{-1} is $\mathcal{O}(N^2)$.

3 Applications

In this section, we show applications of mVMC to the superconductivity at the interfaces of the cuprates [32] and the quantum spin liquid in the Kitaev model [36].

3.1 Application to interfaces of cuprates

In the cuprates, it is well known that the high- T_c superconductivity appears by doping carriers into the Mott insulators. Although there are many families of cuprates, it is common that the critical temperatures of superconductivity show dome-like structures as a function of the doping rates [1, 2, 3] as shown in Fig. 2(a). In other words, it is the *common sense* that the critical temperatures are optimized at the specific doping rate.

Recent experiment of the cuprates interfaces by the Božović group [46], however, challenges the common sense in the cuprates. In the experiment, they make the clean interfaces ($\text{La}_2\text{CuO}_4/\text{La}_{2-x}\text{Sr}_x\text{CuO}_4$) between the insulating mother compounds of the cuprates (La_2CuO_4) and the over-doped metallic cuprates ($\text{La}_{2-x}\text{Sr}_x\text{CuO}_4$), and they examine superconducting properties at the interfaces. Although no superconductivity appears both in the mother compound and over-doped cuprates in the bulk solid, they have

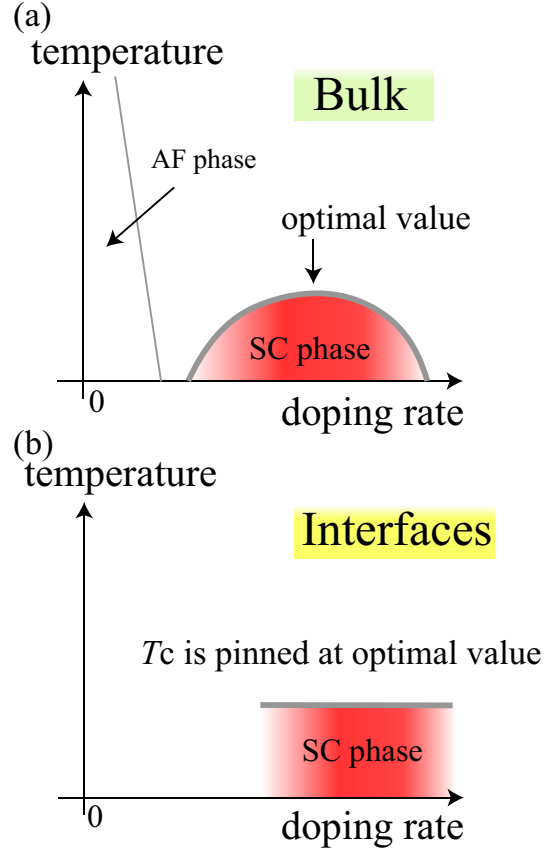


Figure 2: Schematic picture for the experimental phase diagram for (a) bulk solid of the cuprates and (b) interfaces of the cuprates. AF (SC) phase means antiferromagnetic (superconducting) phase.

found that the superconductivity appears at the interfaces of them. They also find that the superconducting temperatures do not depend on the doping rate in the metallic cuprates as is schematically shown in Fig. 2(b). Furthermore, they also show that the superconducting temperature is nearly pinned at the optimal value ($T_c \sim 42\text{K}$) of the bulk cuprates of $\text{La}_{2-x}\text{Sr}_x\text{CuO}_4$. This pinning behavior of T_c is in a sharp contrast with the bulk system where a dome-like doping dependence of T_c has been commonly found in the doping concentration dependence.

To clarify the origin of the unexpected pinning of T_c observed at the interfaces of the cuprate, we analyze the multi-layer Hubbard

model [shown in Fig. 3(a)] by using mVMC, which is one of the simplest theoretical models for the interfaces. The Hamiltonian of the model is given as

$$\begin{aligned}
H = & -t \sum_{\langle i,j \rangle, \sigma, \nu} (c_{i\sigma\nu}^\dagger c_{j\sigma\nu} + \text{h.c.}) \\
& - t_z \sum_{i, \sigma, \langle \nu, \nu' \rangle} (c_{i\sigma\nu}^\dagger c_{i\sigma\nu'} + \text{h.c.}) \\
& + U \sum_{i, \nu} n_{i\uparrow\nu} n_{i\downarrow\nu} - \sum_{i, \sigma, \nu} \epsilon_\nu n_{i\sigma\nu}, \quad (33)
\end{aligned}$$

where $c_{i\sigma\nu}^\dagger$ ($c_{i\sigma\nu}$) is the creation (annihilation) operator of an electron at i th site on the ν th layer with spin σ and $n_{i\sigma\nu} = c_{i\sigma\nu}^\dagger c_{i\sigma\nu}$ is the corresponding number operator. For simplicity, we consider only the nearest-neighbor pair for the intra-layer transfer t and the inter-layer transfer t_z . In this calculation, we consider the five-layer Hubbard model ($0 \leq \nu \leq 4$). We employ the parameter values within the realistic constraint of the cuprate interface suggested from the experimental results and ab initio calculations, i.e., for the inter-layer transfer we take $t_z = 0.05t$ and the onsite Coulomb interaction is set to $U = 8t$. In this analysis, we set the energy unit $t = 1$ (~ 0.5 eV in the cuprates).

The layer-dependent onsite level energy is represented by ϵ_ν . From the experiment, it is known that the inter-layer diffusion of Sr atoms occur around the interfaces [47, 46]. To realistically mimic the inter-layer diffusion effect that makes the onsite energy level gradually change within a few layer, we employ the following layer dependent onsite energy

$$\epsilon_{\nu+1} = \epsilon_\nu - \Delta\epsilon \quad (1 \leq \nu \leq 3), \quad (34)$$

where $\Delta\epsilon$ is a constant. The layer dependence of the onsite level energy is shown in Fig. 3 (b). We assume that the 0th is insulating and the other layers ($\nu \geq 1$) are metallic. To make the 0th layer insulating, we take $\epsilon_0 = \epsilon_1 + 1$.

By using mVMC, we analyze the multi-layer Hubbard model for several choices of $\Delta\epsilon$. We calculate the layer-dependent hole density

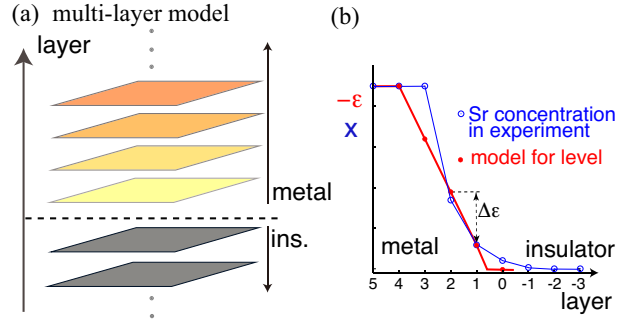


Figure 3: (a) Schematic picture of the theoretical models for the interface of cuprates. The dotted line denotes the interface between the metallic and insulating layer. The color schematically illustrates the change in the carrier concentration obtained by mVMC calculations. (b) Layer dependence of the onsite level energy employed in the multi-layer Hubbard model (red line). In the metallic phase around the interface, we assume that the onsite energy level changes linearly. From this layer-dependence of the onsite level energy, we mimic the effects of interlayer Sr diffusion observed in experiment [47]. We show the layer dependence of the Sr concentration as blue curves, which is taken from Ref. [47]

$\delta_\nu = 1 - N_\nu/N_s$, where N_ν (N_s) is the average electron number of the ν th layer (the number of the sites in each layer). We find that the bulk hole density, $\delta_{\text{bulk}} = \delta_4$, monotonically increases as a function of $\Delta\epsilon$. This result indicates that we can change the doping rate in the metallic region by controlling $\Delta\epsilon$. Thus, we can examine how the changes in the bulk hole density affect the superconducting properties at the interfaces.

To investigate the superconducting properties, we calculate the layer-dependent equal-time superconducting correlations of $d_{x^2-y^2}$

wave symmetry defined as

$$P_\nu(\mathbf{r}) = \frac{1}{2N_s} \sum_{\mathbf{r}_i} \left[\langle \Delta_\nu^\dagger(\mathbf{r}_i) \Delta_\nu(\mathbf{r}_i + \mathbf{r}) \rangle + \text{h.c.} \right], \quad (35)$$

$$\Delta_\nu(\mathbf{r}_i) = \frac{1}{\sqrt{2}} \sum_j f(\mathbf{r}_j - \mathbf{r}_i) (c_{i\uparrow\nu} c_{j\downarrow\nu} - c_{i\downarrow\nu} c_{j\uparrow\nu}), \quad (36)$$

where Δ_ν denotes the $d_{x^2-y^2}$ -wave superconducting order parameter at the ν th layer, $f_d(\mathbf{r})$ is the form factor that describes the $d_{x^2-y^2}$ -wave symmetry, and $\delta_{i,j}$ denotes the Kronecker's delta and $\mathbf{r} = (r_x, r_y)$. To estimate the superconducting long-range order, we calculate long-range limit of $P_\nu(\mathbf{r})$, which is defined as

$$\bar{P}_\nu = \frac{1}{M} \sum_{2 < r = |\mathbf{r}| < \sqrt{2}L} P_\nu(\mathbf{r}). \quad (37)$$

where M is the number of vectors satisfying $2 < r = |\mathbf{r}| < \sqrt{2}L$ (L represents the linear dimension of each layer). For sufficiently large L , this quantity converges to the square of the superconducting order parameter ($|\langle \Delta_\nu^\dagger(\mathbf{r}) \rangle|^2$) and we have actually shown that \bar{P}_ν allows for a practical estimate of the superconducting long-range order in Ref. [20].

In Fig. 4(a), we plot the δ_{bulk} (metallic bulk density) dependence of \bar{P}_ν . As a result, we find that the superconductivity mainly appears at the interface (the 1st layer [$\nu = 1$]). Furthermore, we also find that the superconducting correlations at the interface ($\bar{P}_{\nu=1}$) is nearly fixed to the constant value and we confirm that its constant value is nearly equal to the maximum value in the bulk system, i.e., single-layer Hubbard model. This result is well consistent with experimental results where T_c is pinned at the optimal value in the bulk. We note that the same superconducting order parameter at $T = 0$ naturally yields the same T_c .

In the analysis for the bulk cuprates, if we simply ignore the effects of the long-range Coulomb interactions, we find that the phase separation occurs around half filling and the

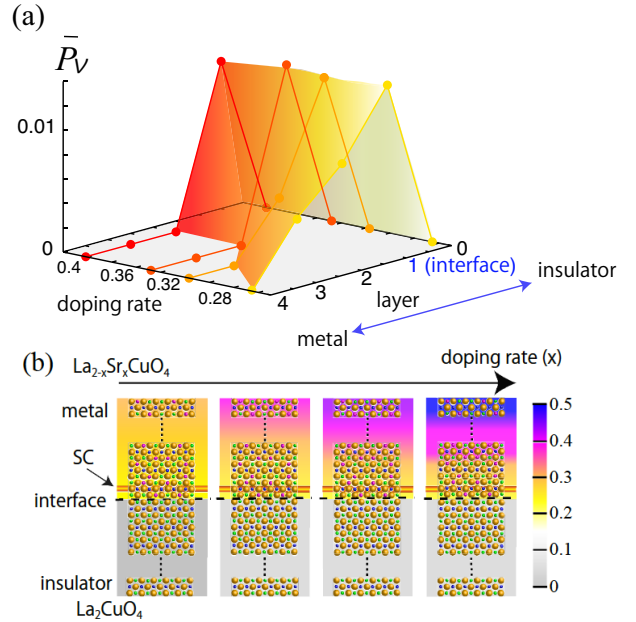


Figure 4: (a) Superconducting correlations for the multi-layer model. Superconducting correlations are pinned at constant value at the interface irrespective of the doping rate in the metallic region. (b) Schematic picture for inter-layer phase separation. The color denote the charge density. Because of the inter-layer degrees of freedom, the instability toward the phase separation in the inner layer is dissolved through the reconstruction of the charge density around the interfaces.

superconducting correlations have maximum value at the edge of the phase separation [48]. By comparing the results for the bulk system and the interfaces, we find that instability toward the phase separation existing in the bulk system is *automatically* dissolved around the interfaces by using the inter-layer degrees of freedom as is schematically shown in Fig. 4(b). In other words, the carrier density at the interfaces is always fixed at the optimal value in the bulk system through the inter-layer phase separation, which dissolves the inner-layer phase separation existing in the bulk system. This result shows that the interfaces provide an ideal tool to stabilize superconductivity without fine tuning of the doping rates.

3.2 Application to the Kitaev model

As an application in the GCE, we perform VMC simulations on the optimization of the ground state in the Kitaev model on the honeycomb lattice [49]. The Kitaev model is defined as

$$\mathcal{H} = \sum_{\gamma=x,y,z} \sum_{\langle I,J \rangle \in \gamma\text{-bond}} K_{\gamma} S_I^{\gamma} S_J^{\gamma}, \quad (38)$$

where I means a site index which includes a unit-cell index i with a degree of freedom of the unit cell $\alpha \in (A, B)$, *i.e.* $I = (i, \alpha)$. Kitaev proved that the ground state of the Kitaev model can be analytically obtained and it is the quantum spin liquid. In addition, for the isotropic Kitaev model, non-Abelian anyons emerge as the elementary excitation by applying magnetic fields, which are important for the realization of the topological quantum computing. Although it seems to be artificial for the Ising interactions to have the dependence on the bond direction, it was theoretically proposed that the Kitaev interaction is dominant in strongly correlated materials with strong spin-orbit coupling [50]. Inspired from this proposal, many researchers have tried to synthesize Kitaev-like compounds and understand how the Kitaev spin liquid can stably exist.

One of the analytical ways to solve the Kitaev model is to use the Jordan-Wigner (JW) transformation. It was shown that the original spin Hamiltonian can be mapped onto the spinless BCS Hamiltonian with many-body interaction on z -bond by using the JW transformation defined as

$$S_j^+ = \prod_{k < j} (-2S_k^z) c_j^{\dagger}, \quad (39)$$

$$S_j^z = (n_j - \frac{1}{2}), \quad (40)$$

and its ground state can be described as the BCS wavefunction[51, 52]. The fermionized

Kitaev model by the JW is represented as

$$\begin{aligned} \mathcal{H} = & \frac{J_x}{4} \sum_i (c_{iA}^{\dagger} - c_{iA})(c_{iB}^{\dagger} + c_{iB}) \\ & + \frac{J_y}{4} \sum_i (c_{iB}^{\dagger} + c_{iB})(c_{i+e_1,A} - c_{i+e_1,A}^{\dagger}) \\ & + \frac{J_z}{4} \sum_i (2n_{iB} - 1)(2n_{i+e_2,A} - 1) \\ & + \mathcal{H}_{\text{boundary}}, \end{aligned} \quad (41)$$

where e_1 and e_2 are primitive translation vectors for the honeycomb lattice. We clearly see that there are the BCS terms, $c_i^{\dagger} c_j^{\dagger}$ and $c_i c_j$, in Eq. (41). $\mathcal{H}_{\text{boundary}}$ means the boundary term which includes string operators due to the application of the JW transformation. When the system satisfies the open boundary condition, this term is banished and thus the original model defined in Eq. (38) can be exactly mapped onto the fermionized one.

Figure 5 shows the optimization process of VMC calculations in the antiferromagnetic Kitaev model by using two different basis; the original spin basis and JW fermion basis. Both are obtained by using a random initial state which has the lowest energy at the 4000 SR step in ten random states. We also perform the ED simulation by using open-source software $\mathcal{H}\Phi$ [53], whose result is shown as the black thin line in Fig. 5. It is clearly seen that the JW fermion result converges to the exact ground state. On the other hand, although the energy by the conventional spin-basis wave function is gradually decreased, it does not seem to reach to the true ground state. This result indicates that the JW fermion basis is more appropriate for obtaining the Kitaev spin liquid without falling into local minima during the optimization process.

4 Summary

In this report, we first explained the basics of mVMC. We explained that mVMC can treat the general Hamiltonians with the arbitrary

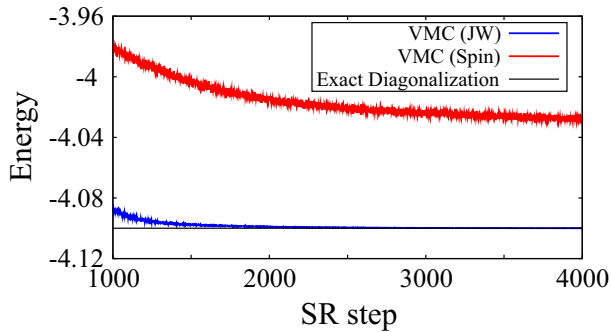


Figure 5: Optimization process in the antiferromagnetic Kitaev model for 4×3 unit cell and $J_x = J_y = J_z = 1$. Red and blue lines show the results by using Eqs. (8) and (9), respectively. Black thin line represents the energy obtained by using the exact diagonalization method.

one-body part and the arbitrary two-body interactions. We also explained the Monte Carlo sampling used in mVMC and the wavefunction implemented in mVMC. We also explained two optimization methods; the steepest descent (SD) method and the stochastic reconfiguration (SR) method. By taking the Hubbard model as an example, we showed that the speed of the optimization by the SD method is slower than that of the SR method. We also detailed the recent extension of mVMC for treating the systems without particle-number conservation

Then, we showed two recent application of mVMC. One is the application to the interfaces of the cuprates. By solving the multi-layer Hubbard model, which is an effective model for the interfaces the cuprates, we showed that the pinning of the T_c observed in the experiment can be well reproduced. We also clarified the origin of the pinning is the inter-layer phase separation. This result indicates that interfaces of the high- T_c superconductors offers an ideal platform for stabilizing optimal superconductivity without fine tuning of the doping rate.

Another application is the analysis of the Kitaev model. By performing the Jordan-Wigner

transformation, it is known that the Kitaev model is exactly solved and the quantum spin liquid appears. There is, however, the anomalous part, which breaks the particle number conservation, inevitably appears. To treat the Kitaev model under the Jordan-Wigner transformation, we used mVMC with the grand canonical ensemble. As a result, mVMC with the grand canonical ensemble works well for reproducing the Kitaev spin liquid.

Acknowledgment

This work was supported by Grant-in-Aid for Building of Consortia for the Development of Human Resources in Science and Technology from the MEXT of Japan. A part of the numerical calculation of this work was performed with the supercomputer in the Institute for Solid State Physics, the University of Tokyo. We also thank the computational resources of the K computer provided by the RIKEN Advanced Institute for Computational Science through the High Performance Computing Infrastructure System Research projects (hp140215, hp150211, hp150173, and hp160201) supported by the MEXT of Japan. This work was also supported by JSPS KAKENHI (Grant Nos. 16K17746 and 16H06345), and by MEXT as a social and scientific priority issue (Creation of new functional devices and high-performance materials to support next-generation industries) to be tackled by using post-K computer. The authors acknowledge Satoshi Morita, Kazuyoshi Yoshimi, Mitsuaki Kawamura, Takahiro Ohgoe, Masatoshi Imada, and Takeo Kato for collaborations in developing mVMC. The work on the interfaces of the cuprates was done by collaboration with Yusuke Nomura, Silke Biermann, and Masatoshi Imada.

References

- [1] M. Imada, A. Fujimori, Y. Tokura, *Rev. Mod. Phys.* **70**, 1039 (1998).
- [2] P. A. Lee, N. Nagaosa, X.-G. Wen, *Rev. Mod. Phys.* **78**, 17 (2006).
- [3] B. Keimer, S. A. Kivelson, M. R. Norman, S. Uchida, J. Zaanen, *Nature* **518**, 179 (2015).
- [4] L. Balents, *Nature* **464**, 199 (2010).
- [5] C. Gros, *Ann. Phys.* **189**, 53 (1989).
- [6] F. Becca, S. Sorella, *Quantum Monte Carlo approaches for correlated systems*, Cambridge University Press, 2017.
- [7] W. L. McMillan, *Phys. Rev.* **138**, A442 (1965).
- [8] D. Ceperley, G. V. Chester, M. H. Kalos, *Phys. Rev. B* **16**, 3081 (1977).
- [9] S. Sorella, *Phys. Rev. B* **64**, 024512 (2001).
- [10] S. Sorella, M. Casula, D. Rocca, *J. Chem. Phys.* **127**, 014105 (2007).
- [11] E. Neuscamman, C. J. Umrigar, G. K.-L. Chan, *Phys. Rev. B* **85**, 045103 (2012).
- [12] <https://github.com/issp-center-dev/mVMC>
- [13] <https://ma.issp.u-tokyo.ac.jp/en/app/518>
- [14] T. Misawa, S. Morita, K. Yoshimi, M. Kawamura, Y. Motoyama, K. Ido, T. Ohgoe, M. Imada, T. Kato, *Computer Physics Communications* **235**, 447 (2019).
- [15] <http://www.issp.u-tokyo.ac.jp/supercom/softwaredev>
- [16] D. Tahara, M. Imada, *J. Phys. Soc. Jpn.* **77**, 114701 (2008).
- [17] D. Tahara, M. Imada, *J. Phys. Soc. Jpn.* **77**, 093703 (2008).
- [18] R. Kaneko, S. Morita, M. Imada, *J. Phys. Soc. Jpn.* **83**, 093707 (2014).
- [19] S. Morita, R. Kaneko, M. Imada, *J. Phys. Soc. Jpn.* **84**, 024720 (2015).
- [20] T. Misawa, M. Imada, *Phys. Rev. B* **90**, 115137 (2014).
- [21] H.-H. Zhao, K. Ido, S. Morita, M. Imada, *Phys. Rev. B* **96**, 085103 (2017).
- [22] K. Ido, T. Ohgoe, M. Imada, *Phys. Rev. B* **97**, 045138 (2018).
- [23] Y. Motome, K. Nakamikawa, Y. Yamaji, M. Udagawa, *Phys. Rev. Lett.* **105**, 036403 (2010).
- [24] T. Misawa, J. Yoshitake, Y. Motome, *Phys. Rev. Lett.* **110**, 246401 (2013).
- [25] T. Misawa, K. Nakamura, M. Imada, *J. Phys. Soc. Jpn.* **80**, 023704 (2011).
- [26] T. Misawa, K. Nakamura, M. Imada, *Phys. Rev. Lett.* **108**, 177007 (2012).
- [27] T. Misawa, M. Imada, *Nat. Commun.* **5**, 5738 (2014).
- [28] M. Hirayama, T. Misawa, T. Miyake, M. Imada, *J. Phys. Soc. Jpn.* **84**, 093703 (2015).
- [29] H. Shinaoka, T. Misawa, K. Nakamura, M. Imada, *J. Phys. Soc. Jpn.* **81**, 034701 (2012).
- [30] M. Hirayama, T. Misawa, T. Ohgoe, Y. Yamaji, M. Imada, *arXiv:1901.00763* (2019).
- [31] T. Ohgoe, M. Hirayama, T. Misawa, K. Ido, Y. Yamaji, M. Imada, *arXiv:1902.00122* (2019).
- [32] T. Misawa, Y. Nomura, S. Biermann, M. Imada, *Sci. Adv.* **2**, e1600664 (2016).

- [33] Y. Yamaji, M. Imada, Phys. Rev. B **83**, 205122 (2011).
- [34] M. Kurita, Y. Yamaji, S. Morita, M. Imada, Phys. Rev. B **92**, 035122 (2015).
- [35] M. Kurita, Y. Yamaji, M. Imada, Phys. Rev. B **94**, 125131 (2016).
- [36] K. Ido, T. Misawa, in preparation.
- [37] T. Ohgoe, M. Imada, Phys. Rev. B **89**, 195139 (2014).
- [38] T. Ohgoe, M. Imada, Phys. Rev. Lett. **119**, 197001 (2017).
- [39] K. Ido, T. Ohgoe, M. Imada, Phys. Rev. B **92**, 245106 (2015).
- [40] K. Ido, T. Ohgoe, M. Imada, Sci. Adv. **3**, e1700718 (2017).
- [41] K. Takai, K. Ido, T. Misawa, Y. Yamaji, M. Imada, J. Phys. Soc. Jpn. **85**, 034601 (2016).
- [42] <https://github.com/issp-center-dev/mVMC-tutorial>
- [43] <http://www.math.sci.hiroshima-u.ac.jp/~m-mat/MT/SFMT>
- [44] G. Carleo, F. Becca, M. Schiró, M. Fabrizio, Sci. Rep. **2**, 243 (2012).
- [45] S.-I. Amari, Neural computation **10**, 251 (1998).
- [46] J. Wu, O. Pelleg, G. Logvenov, A. T. Bollinger, Y.-J. Sun, G. S. Boebinger, M. Vanetić, Z. Radović, I. Božović, Nat. Mat. **12**, 877 (2013).
- [47] G. Logvenov, A. Gozar, I. Božović, Science **326**, 699 (2009).
- [48] T. Misawa, M. Imada, Phys. Rev. B **90**, 115137 (2014).
- [49] A. Kitaev, Ann. Phys. (N. Y). **321**, 2 (2006).
- [50] G. Jackeli, G. Khaliullin, Phys. Rev. Lett. **102**, 017205 (2009).
- [51] X.-Y. Feng, G.-M. Zhang, T. Xiang, Phys. Rev. Lett. **98**, 087204 (2007).
- [52] H.-D. Chen, Z. Nussinov, J. Phys. A Math. Theor. **41**, 075001 (2008).
- [53] M. Kawamura, K. Yoshimi, T. Misawa, Y. Yamaji, S. Todo, N. Kawashima, Comput. Phys. Commun. **217**, 180 (2017).